Supporting Information

Insights into the Interface Reaction Between Electrolyte and Li_2MnO_3 from Ab Initio Molecular Dynamics Simulations

Xiaotong Yan,[a] Chunwei Zhu,[a] Weijie Huang,[a] and Yu-Jun Zhao*[ab]

[a] *Department of Physics, South China University of Technology, Guangzhou 510641, PR China*

[b] *Key Laboratory of Advanced Energy Storage Materials of Guangdong Province, South China University of Technology, Guangzhou 510641, China*

S1. Interface model building

S1.1. The stable Li ion cluster of the electrolyte

The electrolyte cluster structure of the Li ion plays an important role in determining the physicochemical properties of liquid electrolytes.[1-5] In this work, ethylene carbonate (EC), dimethyl carbonate (DMC), and lithium hexafluorophosphate ($LiPF_6$) are used for the composition of the liquid electrolyte cluster. Due to the complexity of electrolyte cluster structures and computational costs, we only consider the nearest neighbor coordination of the Li ion electrolyte cluster. The structure information of EC, DMC, and $LiPF_6$ molecules are shown in Figure S1.

* Corresponding author.
E-mail address: zhaoyj@scut.edu.cn (Y.-J. Zhao).

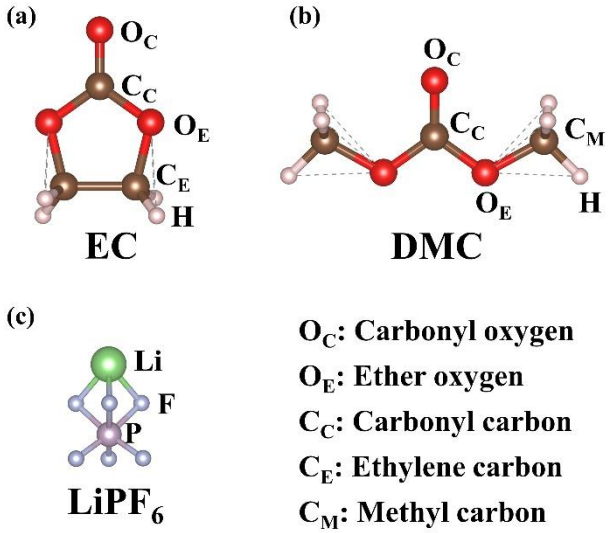

Figure S1. The structure information of EC, DMC, and $LiPF_6$ molecules.

S1.1.1. Computational method

The composition of electrolyte cluster is very complex. Therefore, the software package ABCluster, which is based on the artificial bee colony algorithm, is used to perform a global search for the configuration of molecular clusters at this work.[6, 7] First, the 3000 configurations are searched for each desired molecular cluster (coordination number more than 2) to ensure the reliability of results as much as possible. Then, the xTB method is used to optimize the screened structures to obtain the cluster structure with the lowest energy.[8] To obtain reliable energy data, VASP is used in this work for more accurate energy calculations of the selected most stable Li^+ cluster structure. The van der Waals (vdW) interaction (DFT-D3 method of Becke-Johnson[9]) and cutoff energy option of 600 eV are used. The ionic positions are relaxed until the forces on each ion converge to less than 0.01 eV $Å^{-1}$.

S1.1.2. The coordination number of Li^+ electrolyte cluster

For the accuracy of the calculation, it is assumed that the maximum coordination

number of Li^+ cluster is six. However, only the reasonable structures with six EC/DMC coordinates and four PF_6^- coordinates for Li^+ electrolyte clusters are obtained by cluster screening with ABCluster. The schematic representations of stable Li^+ cluster structures are shown in Figures S2 - S4 (the stable cluster structures from Section 1.1.1).

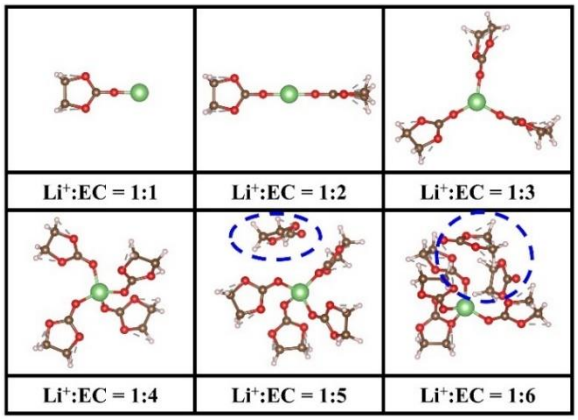

Figure S2. The stable clusters with EC ligand.

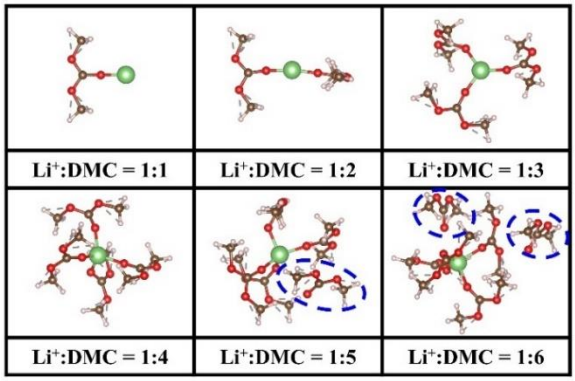

Figure S3. The stable clusters with DMC ligand.

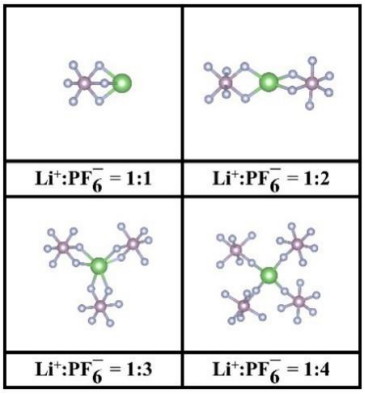

Figure S4. The stable clusters with PF_6^- ligand.

First, the binding energies E_b of the Li^+ cluster with different coordination numbers in single-phase molecule are investigated according to formulas (S1) - (S4).

$$Li^+ + n\mathrm{EC} \leftrightarrow Li^+(\mathrm{EC})_n \quad n \leq 6 \tag{S1}$$

$$Li^+ + n\mathrm{DMC} \leftrightarrow Li^+(\mathrm{DMC})_n \quad n \leq 6 \tag{S2}$$

$$Li^+ + n(PF_6^-) \leftrightarrow Li^+(PF_6^-)_n \quad n \leq 4 \tag{S3}$$

$$E_b = E_{clu} - E_{Li^+} - nE_{mol} \tag{S4}$$

E_{clu} is the total energy of the Li^+ electrolyte cluster. E_{mol} is the energy of the corresponding EC, DMC, and PF_6^- isolated molecules. n is the number of coordination molecule. In addition, E_{Li^+} is the total energy of the Li ion, which is defined as $E_{Li^+} = E_{Li} + E_I$. E_{Li} and E_I are the energy of Li atom and its first ionization energy, respectively. The results of binding energy E_b are shown in Figure S5.

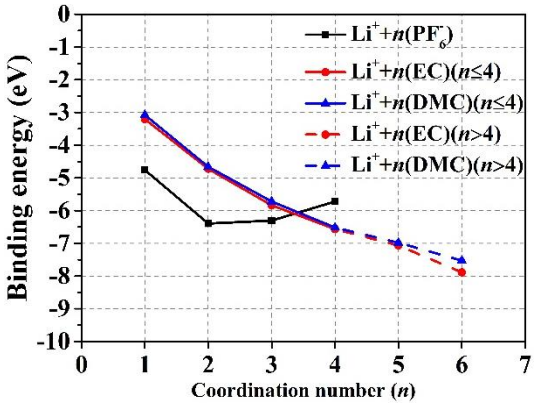

Figure S5. The binding energies E_b of the Li^+ cluster with different coordination molecules and numbers.

Figure S5 shows that the binding energies for the coordination molecules EC or DMC exhibit a monotonic downward trend with increasing coordination number. However, when the coordination number is greater than 4, non-nearest neighbor coordination occurs, as shown in Figures S2 and S3 (blue dotted circle). This indicates that the stable coordination number of Li^+ electrolyte cluster with EC or DMC as

ligands is 4. For the $Li^+(PF_6^-)_n$ cluster, although the stable molecular cluster structure is $Li^+(PF_6^-)_2$, the nearest neighbor Li^+ coordination number is still 4 (four fluorine ions, see Figure S4). In summary, the most stable coordination number of Li^+ electrolyte cluster is 4, which is consistent with the relevant studies.[1-5]

S1.1.3. The stable cluster of Li^+ in EC and DMC mixed under 4 coordination condition

In the case of determined 4 coordination, the binding energies E_b of Li^+ electrolyte cluster with different EC and DMC ratios in EC and DMC mixed are calculated according to the formulas (S5) and (S6). The required cluster structure is screened according to the calculation method in Section S1.1.1. The schematic diagram of corresponding stable Li^+ electrolyte cluster structure is shown in Figure S6.

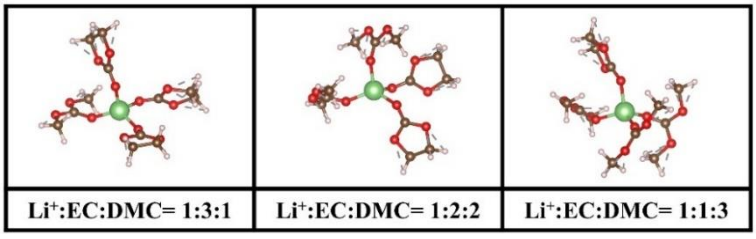

Figure S6. The schematic diagram of Li^+ electrolyte cluster with different ratios of EC:DMC.

$$Li^+ + n\text{EC} + (4\text{-}n)\text{DMC} \leftrightarrow Li^+(\text{EC})_n(\text{DMC})_{4\text{-}n} \quad \text{(S5)}$$

$$E_b = E_{Li^+(\text{EC})_n(\text{DMC})_{4-n}} - E_{Li^+} - nE_{\text{EC}} - (4-n)E_{\text{DMC}} \quad \text{(S6)}$$

The $E_{Li^+(\text{EC})_n(\text{DMC})_{4\text{-}n}}$ is the total energy of the Li^+ cluster with the corresponding ratio of EC:DMC. E_{Li^+} is the energy of the Li ion. E_{EC} and E_{DMC} are the energy of EC and DMC isolated molecules, respectively. In addition, n is the number of the coordination molecule of the EC. The results of binding energy E_b are shown in Figure S7.

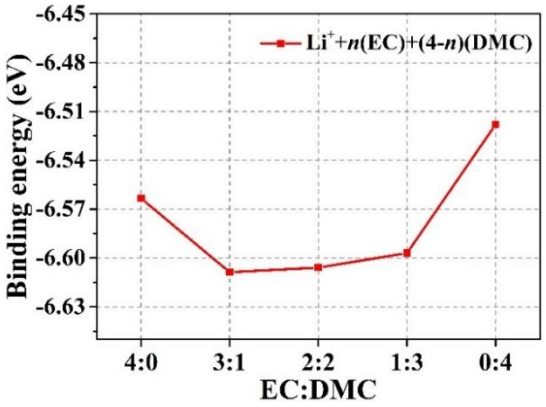

Figure S7. The binding energies E_b of Li^+ cluster with different ratios of EC:DMC.

It can be seen from Figure S7 that the binding energies of mixed-molecular Li^+ clusters are lower than that of single-phase molecular clusters. The Li^+ mixed-molecular cluster of $Li^+(EC)_3(DMC)$ is the most stable structure. In addition, it also can be seen from Figure S7 that the relatively similar binding energy of Li^+ clusters may imply the possibility of interconversion of these Li^+ electrolyte clusters with different ratios of EC:DMC.

S1.1.4. The stable cluster of Li^+ in EC, DMC, and PF_6^- mixed under 4 coordination condition

In addition to the presence of solvent molecules EC and DMC in the liquid electrolyte, lithium salts also must be added to enable the effective migration of Li ions. Therefore, the stability of 4-coordinated Li^+ cluster in the EC/DMC system with lithium salt $Li^+(PF_6^-)$ is also considered in this study (the corresponding stable cluster structures from Section 1.1.1 are shown in Figure S8). The binding energies E_b of stable Li^+ cluster with different ratios of EC:DMC:PF_6^- are calculated according to the formulas (S7) and (S8). It should be noted that due to the ratio of composition of liquid electrolyte given in the main text and in section S1.3. It is assumed that there is only

one PF_6^- molecule in the Li^+ electrolyte cluster.

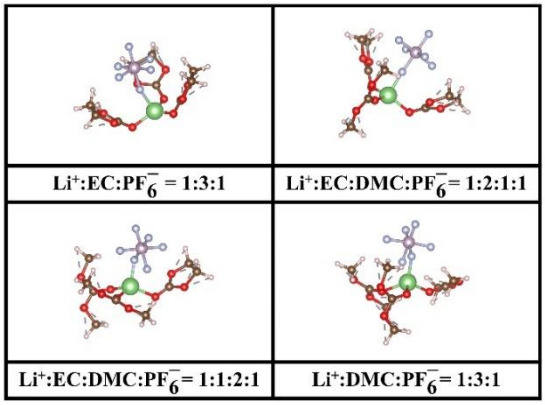

Figure S8. The schematic diagram of Li^+ electrolyte cluster with different ratios of EC:DMC:PF_6^-.

$$Li^+ + n\text{EC} + (3\text{-}n)\text{DMC} + PF_6^- \leftrightarrow Li^+(\text{EC})_n(\text{DMC})_{3\text{-}n}(PF_6^-) \quad \text{(S7)}$$

$$E_b = E_{Li^+(\text{EC})_n(\text{DMC})_{3-n}(PF_6^-)} - E_{Li^+} - nE_{\text{EC}} - (3-n)E_{\text{DMC}} - E_{PF_6^-} \quad \text{(S8)}$$

The $E_{Li^+(\text{EC})_n(\text{DMC})_{3\text{-}n}(PF_6^-)}$ is the total energy of Li^+ cluster with the corresponding ratio of EC:DMC:PF_6^-. The E_{Li^+} is the energy of the Li ion. The E_{EC}, E_{DMC}, and $E_{PF_6^-}$ are the energy of EC, DMC, and PF_6^- isolated molecules, respectively. In addition, n is the number of the coordination molecule of EC. The results of binding energy E_b are shown in Figure S9.

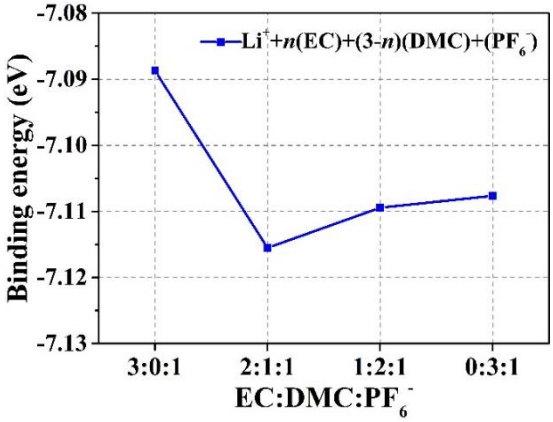

Figure S9. The binding energies E_b of Li^+ cluster with different ratios of EC:DMC:PF_6^-.

Figure S9 shows that the electrolyte cluster $Li^+(\text{EC})_2(\text{DMC})(PF_6^-)$ has the lowest binding energy. This is consistent with the relevant studies.[5, 10] In addition, it can be

seen from Figure S9 that the relatively similar binding energies of Li^+ electrolyte cluster with different ratios of EC:DMC:PF_6^- also imply the possibility of mutual conversion of these difference electrolyte clusters.

S1.1.5. The stability of Li^+ electrolyte clusters

According to the discussion in Sections S1.1.2, S1.1.3, and S1.1.4, the stable electrolyte clusters are $Li^+(PF_6^-)_2$, $Li^+(EC)_3(DMC)$, and $Li^+(EC)_2(DMC)(PF_6^-)$, respectively. Based on the above stable electrolyte clusters, the formation energies E_f of various stable Li^+ electrolyte cluster under 4 coordination are calculated according to the formulas (S9) - (S12).

$$2Li^+(PF_6^-) + 6EC + 2DMC \leftrightarrow Li^+(PF_6^-)_2 + Li^+(EC)_3(DMC) + DMC + 3EC \quad (S9)$$

$$2Li^+(PF_6^-) + 6EC + 2DMC \leftrightarrow 2Li^+(EC)_3(DMC) + 2PF_6^- \quad (S10)$$

$$2Li^+(PF_6^-) + 6EC + 2DMC \leftrightarrow 2Li^+(EC)_2(DMC)(PF_6^-) + 2EC \quad (S11)$$

$$E_f = E_{product} - E_{reactant} \quad (S12)$$

The $E_{product}$ is the total energy of the product, and $E_{reactant}$ is the total energy of the reactant. According to the calculation, the formation energies obtained by equations (9), (10), and (11) are -3.488 eV, -3.702 eV, and -4.716 eV, respectively, indicating that $Li^+(EC)_2(DMC)(PF_6^-)$ is the most stable electrolyte cluster in the liquid electrolyte.

To summarize, the coordination number of nearest electrolyte molecule around Li ion is 4. The electrolyte cluster $Li^+(EC)_2(DMC)(PF_6^-)$ is the most stable electrolyte cluster. At the same time, the binding energy shows that there are possibilities of interconversion between Li-ion electrolyte clusters with different electrolyte molecular proportions.

S1.2. The typical surfaces of Li_2MnO_3

In this study, the typical surfaces of Li_2MnO_3 are (001), (010), $(10\bar{1})$, and (131), respectively, drawing on our previous research.[11] The structure diagram of corresponding surfaces is shown in Figure S10.

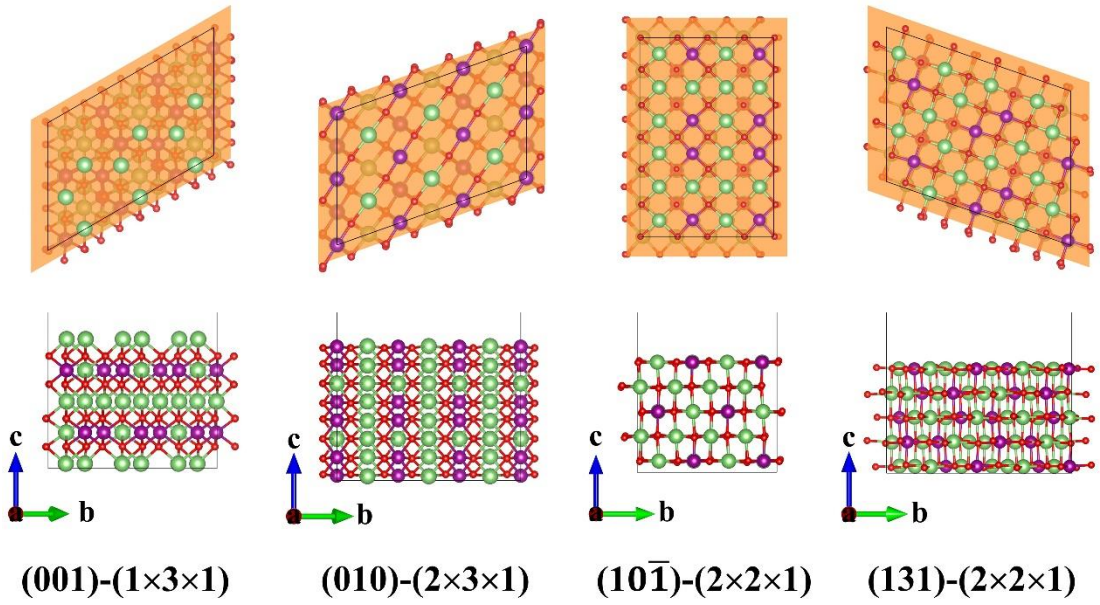

Figure S10. The structural diagram of the (001), (010), $(10\bar{1})$, and (131) surfaces (green: Li; purple: Mn; red: O).

According to our previous study, the stoichiometric surfaces of $(10\bar{1})$ and (131) (similar surface energy) have the lowest surface energies compared to other surfaces. The surface energy of the stoichiometric surface of (001) is relatively higher than that of the $(10\bar{1})$ and (131) surfaces. However, it is difficult for Li_2MnO_3 grain to grow rapidly along the [001] direction due to the high barrier. As a result, it grows rapidly in the direction parallel to the (001) plane and does not significantly increase the total energy of the system. Therefore, the (001) surface is found as the main surface for Li_2MnO_3.[12, 13] Moreover, the (010) surface of manganese-rich terminal shows the best oxygen suppression properties compared to other surfaces. Thus, the interface reactions

of (001), (010), $(10\bar{1})$, and (131) surfaces with liquid electrolyte are mainly investigated in this work.

S1.3. The parameters of interface model building

Firstly, according to the electrolyte ratio information in the main text, the molecular numbers of EC, DMC, and LPF_6 in the electrolyte used in this paper are 7, 6, and 1, respectively (i.e. EC: DMC: $Li^+(EC)_2(DMC)(PF_6^-)$ = 5: 5: 1). This is based on the density properties (see Table S1) of the electrolyte molecule and the available computational resources.

Table S1. The density information for different electrolyte molecules.

Electrolyte	Density (g cm^{-3})	Volume ($Å^3$)	Number
EC	1.32	110.70	7
DMC	1.07	139.67	6
$LiPF_6$	1.50	88.82	1

In order to better observe the interface reaction between the surface and the liquid electrolyte. The slab structures of Li_2MnO_3 surface are treated by cell expansion. The details of slab structure are shown in Table S2 and Figures S10 and S11.

Table S2. The parameters of interface model building.

Surface	*x* (Å)	*y* (Å)	*γ* (°)	Area ($Å^3$)	*z* (Å)
(001)-(1×3×1)	9.99	12.99	119.91	129.74	13.11
(010)-(2×3×1)	10.00	14.36	109.48	143.63	11.85
$(10\bar{1})$-(2×2×1)	17.29	11.64	90.00	201.24	8.46
(131)-(2×2×1)	13.00	15.55	70.90	202.20	8.42

Finally, based on the information about the surface structures (e.g. lattice constant and surface area) and the electrolyte molecules (e.g. volume and number), we created

the interface model. The distribution of electrolyte molecules in the interface model is randomly generated by the software PACKMOL.[14] In addition, according to the relevant references,[10, 15] the atomic layer of He atoms is used to avoid the reaction between electrolyte and bulk for periodic reasons. The interface model is shown in Figure S11.

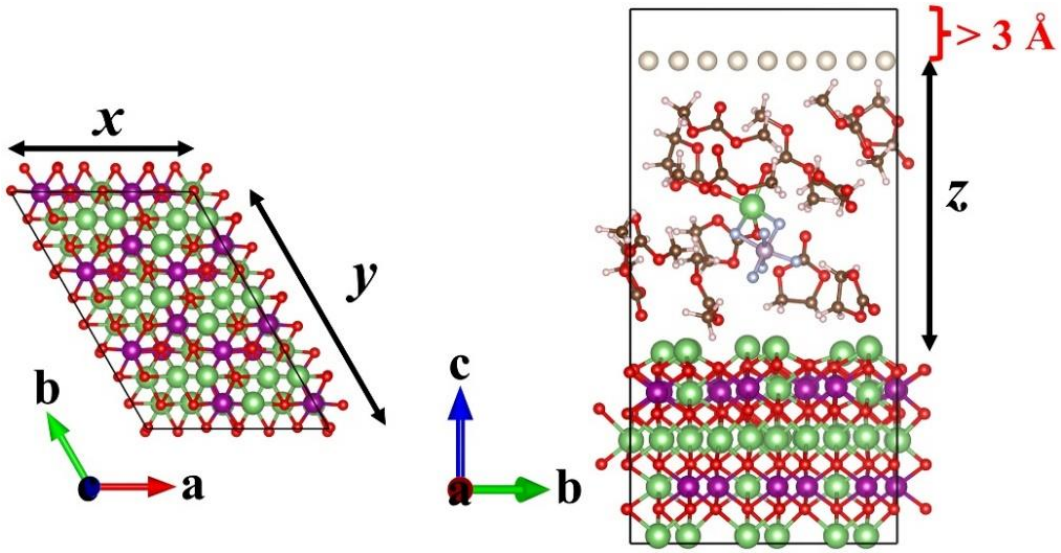

Figure S11. The schematic diagram of interface model (the interface model of the (001) surface as an example).

S2. Binding determination

The process of the interface reaction involves the breaking of existing bonds and the subsequent formation of new bonds. In this study, a criterion for determining the presence of a bond between atoms is established. The AIMD calculations only show fission and binding processes involving C-O, Mn-O, and Li-O species within the interface model at this work. Therefore, the bond lengths derived from the atomic (ionic) radii under covalent (ionic) bond conditions are compared with the calculated results of corresponding structure. Further details can be seen in Table S3.

Table S3. The comparison of bond lengths in different cases.

	Covalent bond	Ionic bond	Calculation
		Radius (Å)	
C	0.75 (sp^3)	-0.08 (+4, III)	-
O	0.66	1.35(-2, II) or 1.40 (-2, VI)	-
Li	1.28	0.76 (+1, VI)	-
Mn	1.61 (h.s.)	0.53 (+4, VI)	-
		Bond length (Å)	
C-O	1.41	1.27	1.37 (EC: C_C-O_E)
Li-O	1.94	2.16	2.10 (Li_2MnO_3)
Mn-O	2.27	1.93	1.94 (Li_2MnO_3)

* sp^3 is the atomic orbital hybridization of *s* and *p* orbitals

* h.s. is the high spin state

* Numeric is the valence state of difference ions

* Roman numeral is the coordination number of difference ions

According to Table S3, the sum of atomic radii in a covalent bond (1.41 Å) can be used as a criterion for determining the C-O bond (the data for atomic radii in covalent bond are acquired from reference 16). For the Li-O and Mn-O bonds, the sum of ionic radii (2.16 Å and 1.93 Å) can be used as a basis for judgment (the data for the ionic radii come from the Database of the Ionic Radii, see http://abulafia.mt.ic.ac.uk/shannon/ptable.php).

S3. Complete AIMD and CINEB data for different interfaces

S3.1. (010) interface

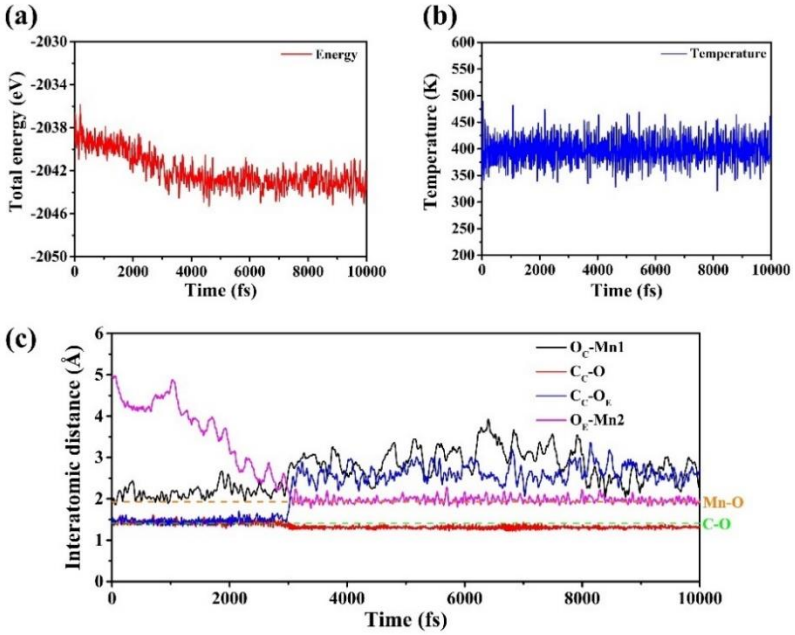

Figure S12. (a) and (b) the changes of energy and temperature with time, and (c) the changes of interatomic distance of EC and (010) surface, in total AIMD simulation.

S3.2. $(10\bar{1})$ interface

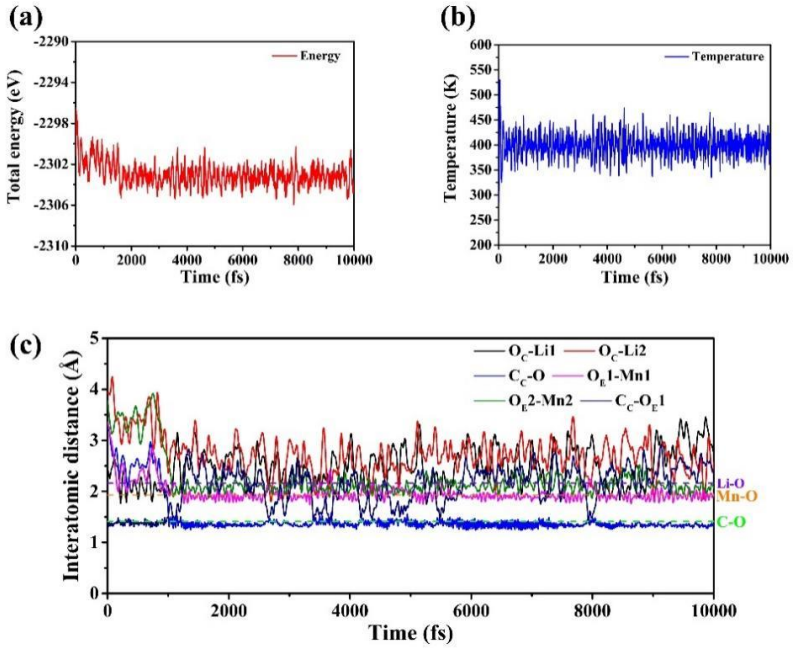

Figure S13. (a) and (b) the changes of energy and temperature with time, and (c) the changes of interatomic distance of EC and $(10\bar{1})$ surface, in total AIMD simulation.

S3.3. (131) interface

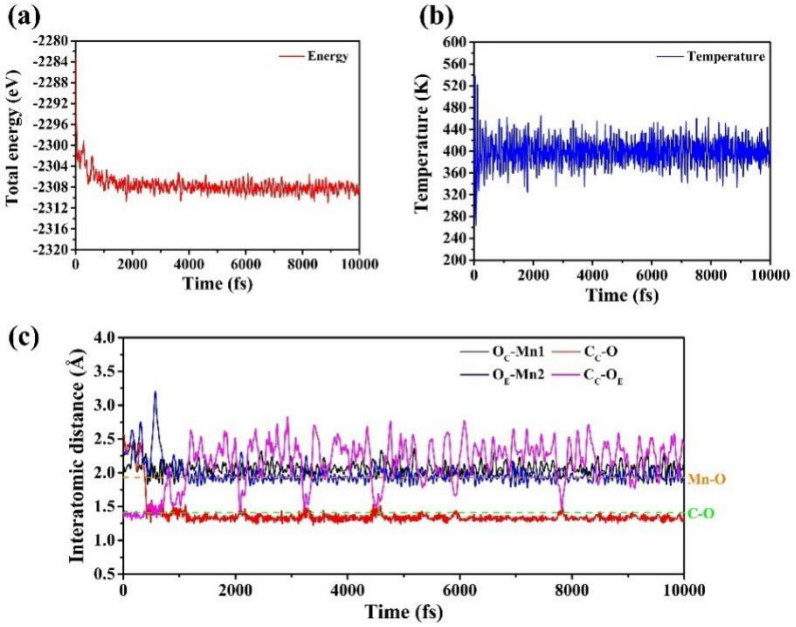

Figure S14. (a) and (b) the changes of energy and temperature with time, and (c) the changes of interatomic distance of EC and (131) surface, in total AIMD simulation.

S3.4. (001) interface

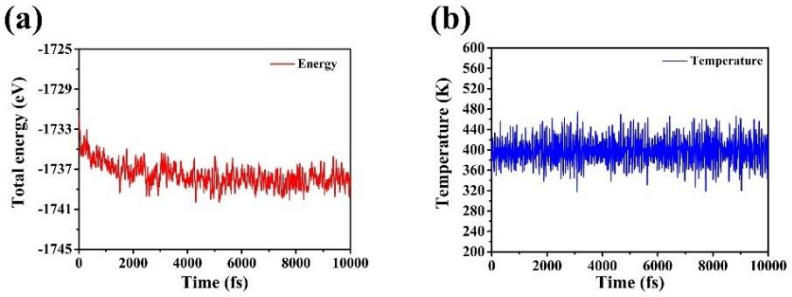

Figure S15. (a) and (b) the changes of energy and temperature with time in total AIMD simulation.

S3.5. Details of the CINEB calculation of EC decomposition on different surfaces

During the AIMD simulation, we observed the decomposition of electrolyte molecules. We then extracted the initial and final states of these decomposition structures and calculated the potential energy barrier using the Climbing Image Nudged

Elastic Band (CINEB) method for the transition state after structural optimization. According to reference 17, the influence of surrounding electrolyte molecules on the potential decomposition barrier is limited. To prevent energy fluctuations caused by interactions with other undecomposed electrolytes from affecting the accuracy of the overpotential calculation, we artificially removed the excess undecomposed electrolyte. The detailed C_C-O_E distances (*d*) and relative energy changes (*ΔE*) during the decomposition of EC molecules on different surfaces are shown in Table S4, corresponding to Figures 2(c), 3(c), and 4(c) in the main text.

Table S4. The *d* (in Å) of C_C-O_E and *ΔE* (in meV) changes during the decomposition of EC molecules on different surfaces by CINEB method.

(010)	*ΔE*	*d*	$(10\bar{1})$	*ΔE*	*d*	(131)	*ΔE*	*d*
0(IS)	0	1.557	0(IS)	0	1.636	0(IS)	0	1.635
1	1.6	1.601	1(TS)	0.2	1.711	1	3.3	1.711
2(TS)	3.7	1.653	2	-2.4	1.803	2(TS)	7.1	1.803
3	-296.6	2.498	3	-55.6	2.171	3	-11.7	2.068
4	-488	2.842	4	-99	2.309	4	-45.5	2.275
5(FS)	-554.7	3.203	5(FS)	-116.3	2.378	5(FS)	-54	2.365
0~2 (Rel.0)	0.6	1.577	0~2 (Rel.0)	0	1.671	0~2 (Rel.0)	1	1.670
	1.6	1.600		0.2	1.711		3.3	1.711
	2.7	1.626		-0.3	1.757		5.7	1.757
2~3 (Rel.2)	-0.2	1.682	EC: C_C-O_E bond	1.37 Å		2~3 (Rel.2)	-0.3	1.869
	-87	2.084					-3.8	1.935
	-221	2.364					-10.3	2.002

* IS, TS, and FS represent the initial, transitional and final states

* Rel.0 and Rel.2 indicate the relative energies respect to the 0 and 2 states

* 0~2 and 2~3 represent the insertion of three migration sites between the 0 and 2 states (2 and 3 states)

As shown in Table S4, we added more embedding points around the TS locations for the CINEB calculations to ensure the accuracy of the results. For the $(10\bar{1})$ and (131) surfaces, the change interval for the C_C-O_E distance is only 0.06 Å due to the

inclusion of more transition points, effectively guaranteeing the validity of the calculation results.

For the (010) surface, the change interval of the C_C-O_E distance between 0 and 2(TS) is only 0.03 Å. However, the C_C-O_E distance for embedding site 1 changes from 1.864 Å to 1.682 Å when the decomposition potential barrier between the 2(TS) and 3 sites is calculated using the CINEB method. The schematic representation can be seen in Figure S16(a). From Table S4, it is evident that insertion site 1 is the highest energy point of the transition state from 2(TS) to 3 on the (010) surface. In the CINEB calculation, the highest energy point is approached with an increasing tendency. Therefore, we extracted the iteration data of this process, and the result is shown in Figure S16(b). The energy variation in Figure S16(b) increases monotonically with decreasing C_C-O_E distance. This indicates that higher energy barriers do not occur within the variation range from 1.653 Å to 1.864 Å (or even 1.875 Å), suggesting that the reaction is spontaneous at this stage.

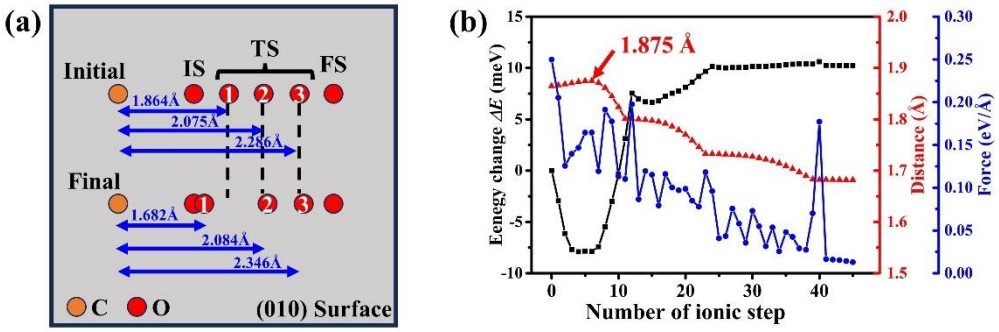

Figure S16. (a) Schematic diagram of the insertion site positions before and after the CINEB calculation. (b) Iteration data for insertion site 1 during the CINEB calculation process.

Since the CINEB method is not suitable for calculating the transition barrier between the 2(TS) and 3 states on the (010) surface, we used the conventional NEB

method to calculate the energy barrier at this stage.[18] The results are shown in Table S5. Combining the data from Tables S4 and S5, the C_C-O_E distances range from 1.864 Å (or even 1.875 Å) to 2.498 Å. The distance between the insertion points of the transition states is only 0.1 Å. In summary, this ensures the reliability of our calculations for the decomposition barriers of electrolyte molecules on the (010) surface.

Table S5. The *d* (in Å) of C_C-O_E and ΔE (in meV) changes during the decomposition of EC molecules on (010) surfaces by NEB method.

(010)	ΔE	*d*
	-45.6	1.981
2~3	-104.7	2.135
(Rel.2)	-164.5	2.262
	-250.5	2.431

* Rel.2 indicate the relative energies respect to the2 states

* 2~3 represent the insertion of three migration sites between the 2 and 3 states

S4. Comparison between work function and HOMO

According to the relevant Refs. 19 and 20, generally speaking, the energy level Φ (the Fermi energy level with respect to the vacuum, i.e. the negative value of the work function) of the cathode material surface should generally be higher than the highest occupied molecular orbital (HOMO) of electrolyte molecule. This is helpful to avoid the spontaneous transfer of electrons in electrolyte molecule to the electrode surface during charging (when Φ is smaller than HOMO). The comparisons of the energy level Φ of different surfaces and the HOMO of different electrolyte molecules are shown in Figure S17.

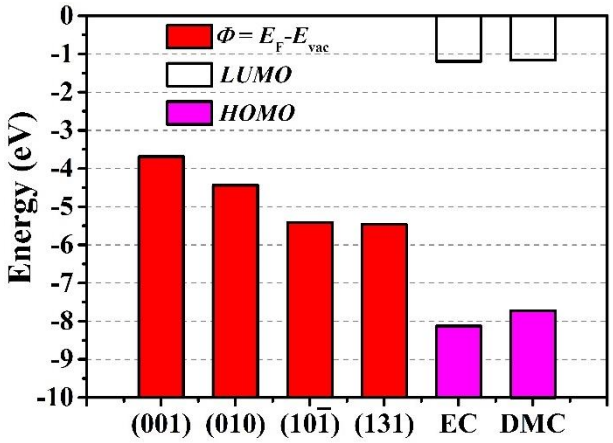

Figure S17. The comparison between the energy level Φ of different surfaces and the HOMOs of EC and DMC molecule.

Figure S17 shows that the energy level Φ at surfaces (001), (010), (10$\bar{1}$), and (131) range from high to low. Compared to the other surfaces, the (001) surface has the largest gap between the surface energy level Φ and the HOMO of electrolyte molecules. This indicates that the (001) surface is less likely to react with the electrolyte than other surfaces. In combination with the above discussion, the main text explanation and the previous work,[11] it shows that surface (001) is an inert surface. Note that the HOMO and LUMO levels of the electrolyte molecule can be estimated from the first adiabatic electron transfer from and to the electrolyte molecule, respectively. The corresponding calculation formulas are (S13) - (S15).

$$\emptyset = E_F - E_{vac} \quad \text{(S13)}$$

$$LUMO = E_{N+1} - E_N \quad \text{(S14)}$$

$$HOMO = E_N - E_{N-1} \quad \text{(S15)}$$

E_F and E_{vac} are the Fermi level and vacuum level of corresponding surface, respectively. E_{N+1}, E_N, and E_{N-1} represent molecular energies with different electron numbers, and N is the electron number of the EC or DMC molecule.

S5. Decomposition of the DMC at (131) interface

The decomposition of DMC molecule on the (131) surface of Li_2MnO_3 is determined by AIMD simulation. In order to clarify the decomposition process of the DMC molecule, the distances between the atoms involved in the reaction process are statistically analyzed. The corresponding results are shown in Figure S18.

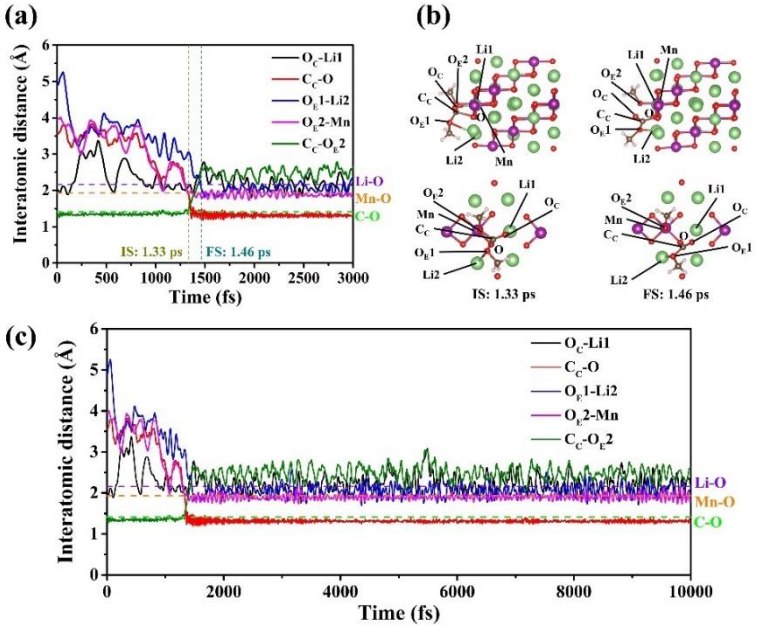

Figure S18. (a) The changes of interatomic distance in the decomposition process of DMC on (131) surface. (b) The schematic diagram of DMC decomposition. (c) The changes of interatomic distance in the decomposition process of DMC on (131) surface at total AIMD simulation.

According to Figure S18, the following behaviors are observed. (i) The O_C of DMC molecule is adsorbed on the Li1 of the (131) surface. (ii) The C_C and O_E2 of the DMC molecule adsorb onto the O and Mn of the (131) surface, respectively. The DMC molecule starts the decomposition reaction at this time (at 1.33 ps). (iii) The distance between C_C and O_E2 gradually increases. (iv) The C_C-O_E2 bond holding breaks at 1.46 ps and beyond.

This reaction process is very similar to the main text (i.e. for the breakage of C_C-

O_E, except that the C_C of the electrolyte molecule is adsorbed on the O of the surface, the O_E must be adsorbed on the Mn of the surface). Note that the information about the decomposition energy barrier and the electronic structure of DMC on the (131) surface cannot be obtained during the decomposition process. This is due to the DMC molecule breaking down during the structure optimization of the adsorption structure. Therefore, we assume that the energy barrier of DMC decomposition is close to zero (similar to the EC ring-opening).

S6. The changes of O_E and Li distance with time

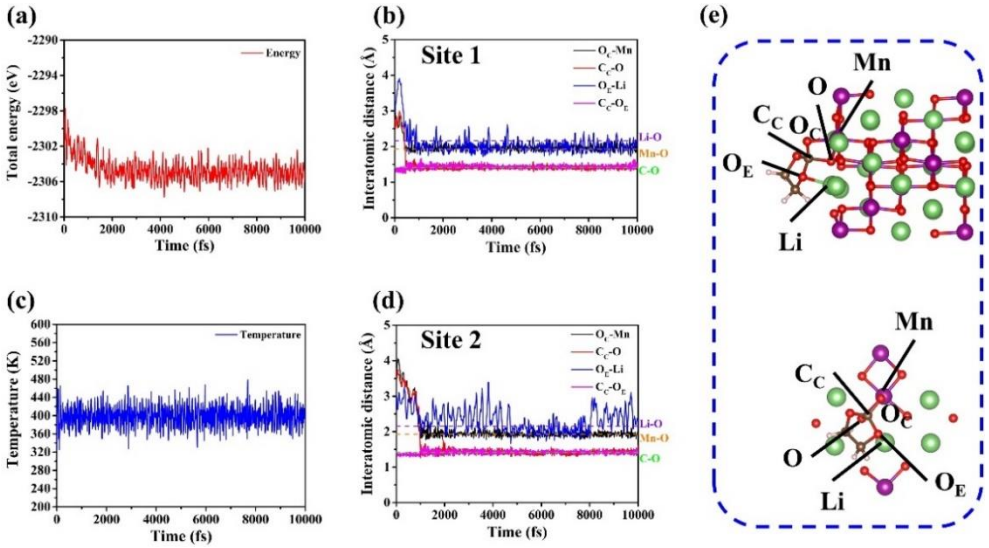

Figure S19. (a) and (c) the changes of energy and temperature with time at the (131) interface. (b) and (d) the changes of interatomic distance of EC and (131) surface with different sites in total AIMD simulation. (e) The schematic diagram of EC molecule adsorption on (131) surface.

From Figures S19(b) and S19(d), it can be seen that the O_C and C_C of the EC molecule and the Mn and O of the (131) surface can be stably bind over time. However, the O_E and Li of the EC molecule and (131) surface at different sites cannot effectively bind (the large energy level gap between the Li^+ of the (131) surface and the O_E of the

EC molecules, see main text), and the bond of C_C-O_E is also unbroken. The EC molecule remain stable in total AIMD simulation. This shows that in the case of C_C-O binding, the adsorption of O_E and Li cannot effectively break the C_C-O_E bond (compared to the adsorption of O_E and Mn). This indicates that the breaking of the C_C-O_E bond requires specific adsorption site.

S7. The influence for vdW interaction

We employed the same liquid electrolyte model to obtain the degree of influence of the vdW interaction on the results to prove that the vdW interaction is negligible.

In this section, we used PACKMOL software to stochastically distribute molecules of EC, DMC, and $Li^+(EC)_2(DMC)(PF_6^-)$ with the respective molecular amounts of 11, 10, and 2 in a 13.00 Å × 15.08 Å × 18.09 Å box (refer to the main text and Section S1.3). The AIMD calculations are performed with the VASP. The NVT ensemble is used at an equilibrium temperature of 400 K for a total time of 20 ps with a time interval of 1 fs. The cutoff energy for the plane wave expansion is set to 400 eV. The convergence criterion for the iteration of the electronic self-consistant is 1×10^{-4} eV. In addition, the gamma point of the Brillouin zone is sampled without consideration of symmetry. The vdW interaction (DFT-D3 method of Becke-Johnson) is used in one of calculations. The outcomes of the calculation are depicted in Figures S20 and S21.

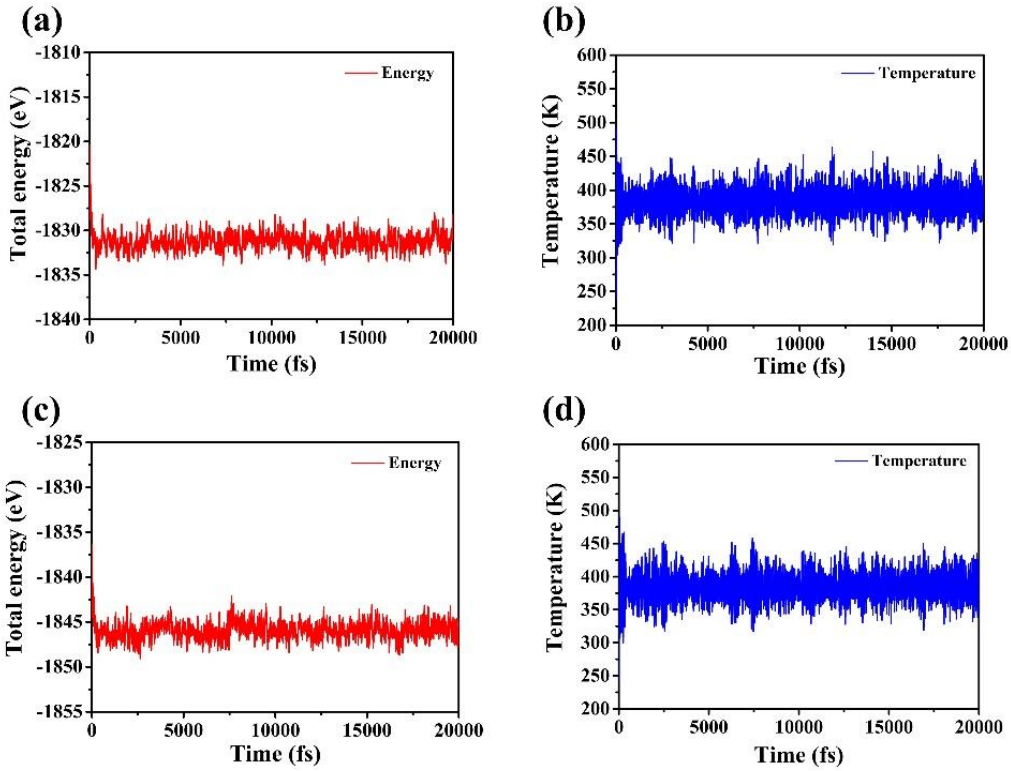

Figure S20. The changes of energy and temperature with time at total AIMD simulation. The (a) and (b) do not consider vdW interaction, and the (c) and (d) consider vdW interaction.

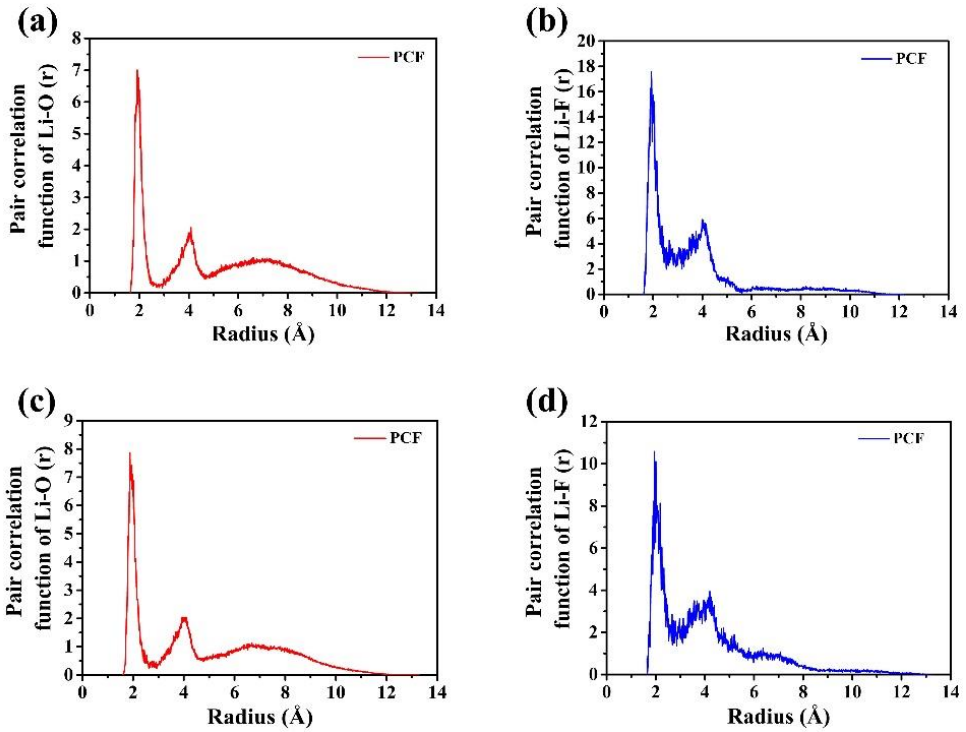

Figure S21. The pair correlation functions (PCFs) of Li-O and Li-F from AIMD simulations. The (a) and (b) do not consider vdW interaction, and the (c) and (d) consider vdW interaction.

The comparison of the pair correlation functions (PCFs) of Li-O and Li-F in Figure S21 indicates that the vdW interaction has no significant effect on the system's results, which are in line with those reported in Ref. 10. Therefore, we have chosen not to consider the vdW interaction in AIMD simulations to save computational costs. A similar result can also be found in Section S8 (the AIMD simulation of the (001) interface).

S8. Descriptions for AIMD animation

Since a large number of AIMD simulations are performed in this paper, the dynamic images accompanying in this study are explained as follows (by OVITO program[21]):

AIMD-I: The AIMD simulation of the interface between electrolyte and (010) surface.

AIMD-II: The AIMD simulation of the interface between electrolyte and $(10\bar{1})$ surface.

AIMD-III: The AIMD simulation of the interface between electrolyte and (131) surface for EC reaction.

AIMD-IV: The AIMD simulation of the interface between electrolyte and (131) surface for DMC reaction.

AIMD-V: The AIMD simulation of the interface between electrolyte and (131) surface for EC unreacted at site 1 (c.f. Section S6).

AIMD-VI: The AIMD simulation of the interface between electrolyte and (131) surface for EC unreacted at site 2 (c.f. Section S6).

AIMD-VII: The AIMD simulation of the electrolyte without vdW interaction.

AIMD-VIII: The AIMD simulation of the electrolyte with vdW interaction.

AIMD-IX: The AIMD simulation of the interface between electrolyte and (001) surface.

AIMD-X: The AIMD simulation of the interface between electrolyte and (001) surface with high calculation accuracy. The vdW interaction (DFT-D3 method of Becke-Johnson) and the cutoff energy option of 500 eV are used. Note that the electrolyte molecules do not react with the (001) surface even with high computational accuracy. This again proves that the (001) surface is an inert surface and also shows that the vdW interaction is negligible.

References

1. K. Chen, X. Shen, L. Luo, H. Chen, R. Cao, X. Feng, W. Chen, Y. Fang and Y. Cao, *Angewandte Chemie International Edition*, 2023, **62**.
2. A. Bhandari, P. K. Gupta, J. Bhattacharya and R. G. S. Pala, *Journal of The Electrochemical Society*, 2019, **166**, A2966-A2972.
3. O. Borodin and G. D. Smith, *The Journal of Physical Chemistry B*, 2009, **113**, 1763-1776.
4. T. A. Pham, K. E. Kweon, A. Samanta, V. Lordi and J. E. Pask, *The Journal of Physical Chemistry C*, 2017, **121**, 21913-21920.
5. I. Skarmoutsos, V. Ponnuchamy, V. Vetere and S. Mossa, *The Journal of Physical Chemistry C*, 2015, **119**, 4502-4515.
6. J. Zhang and M. Dolg, *Physical Chemistry Chemical Physics*, 2015, **17**, 24173-24181.
7. J. Zhang and M. Dolg, *Physical Chemistry Chemical Physics*, 2016, **18**, 3003-3010.
8. C. Bannwarth, E. Caldeweyher, S. Ehlert, A. Hansen, P. Pracht, J. Seibert, S. Spicher and S. Grimme, *WIREs Computational Molecular Science*, 2020, **11**.
9. S. Grimme, S. Ehrlich and L. Goerigk, *Journal of Computational Chemistry*, 2011, **32**, 1456-1465.
10. B. Zhang, Z. Lin, H. Chen, L.-W. Wang and F. Pan, *Journal of Materials Chemistry A*, 2020, **8**, 2613-2617.
11. X. Yan, X. Zhou, C. Zhu, W. Huang and Y.-J. Zhao, *Journal of Materials Chemistry A*, 2024, **12**, 3722-3733.
12. A. Quesne-Turin, D. Flahaut, L. Croguennec, G. Vallverdu, J. Allouche, Y. Charles-Blin, J.-N. Chotard, M. Ménétrier and I. Baraille, *ACS Applied Materials & Interfaces*, 2017, **9**, 44222-44230.
13. X. Yang, W. Tang, H. Kanoh and K. Ooi, *Journal of Materials Chemistry*, 1999, **9**, 2683-2690.
14. L. Martínez, R. Andrade, E. G. Birgin and J. M. Martínez, *Journal of Computational Chemistry*, 2009, **30**, 2157-2164.
15. S. Angarita-Gomez and P. B. Balbuena, *ACS Applied Materials & Interfaces*, 2022, **14**, 56758-56766.

16. B. Cordero, V. Gómez, A. E. Platero-Prats, M. Revés, J. Echeverría, E. Cremades, F. Barragán and S. Alvarez, *Dalton Transactions*, 2008, DOI: 10.1039/b801115j.
17. S. Xu, G. Luo, R. Jacobs, S. Fang, M. K. Mahanthappa, R. J. Hamers and D. Morgan, *ACS Applied Materials & Interfaces*, 2017, **9**, 20545-20553.
18. G. Henkelman and H. Jónsson, *The Journal of Chemical Physics*, 2000, **113**, 9978-9985.
19. J. B. Goodenough and Y. Kim, *Chemistry of Materials*, 2009, **22**, 587-603.
20. M. Gauthier, T. J. Carney, A. Grimaud, L. Giordano, N. Pour, H.-H. Chang, D. P. Fenning, S. F. Lux, O. Paschos, C. Bauer, F. Maglia, S. Lupart, P. Lamp and Y. Shao-Horn, *The Journal of Physical Chemistry Letters*, 2015, **6**, 4653-4672.
21. A. Stukowski, *Modelling and Simulation in Materials Science and Engineering*, 2010, **18**.